PERGAMON

International Journal of Solids and Structures 40 (2003) 25–46

INTERNATIONAL JOURNAL OF SOLIDS and STRUCTURES

www.elsevier.com/locate/ijsolstr

# Nonlinear proportionality of shear-bond stress to shear force in partially plastic regions of asymmetric FRC-laminated steel members

W.M. Sebastian *

*Department of Civil Engineering, University of Bristol, University Walk, Bristol BS8 1TR, UK*

Received 4 March 2002

**Abstract**

This paper focuses on the elastic–plastic flexural characteristics of hybrid members comprising I-section steel beams with adhesively bonded fiber reinforced composite (FRC) laminates. Specifically, predictive models are presented for the shear-bond stresses developed within the adhesive layer. The asymmetry of the hybrid section, due to the presence of the laminate, is shown to have two important consequencies, namely that two parameters are required to fully define the elastic–plastic behavior, and that there is a progressive migration of the neutral axis towards the laminate as elastic–plastic flexure of the section increases. Five different phases of elastic–plastic flexure are identified. Analytically exact two-parameter predictive models, which incorporate the nomadic tendencies of the neutral axis, are derived for the shear-bond stresses associated with each phase. The models reveal that, in contrast to fully elastic flexure, shear-bond stress is nonlinearly proportional to shear force during elastic–plastic behavior. Predictions from the models are compared with test data from the laboratory and with predictions from a finite element program, for FRC-laminated I-section steel beams under both distributed loads and point loads. These comparisons show that two elastic–plastic phases, each defined by axial stress redistribution within the tension steel flange, stimulate rapidly varying shear-bond stresses in the adhesive. The capabilities of the models are highlighted, and areas open for further work are discussed.


*Keywords:* Adhesive; Shear-bond stress; Fiber reinforced composite; Steel; Elastic–plastic; Nonlinear; Finite element

## 1. Introduction

The current economic climate has prompted a shift in attitude towards deficient Civil Engineering structures, from outright replacement of these structures to repair or upgrading of the same. One repair technique which shows great promise involves structural adhesive bonding of sheets of high-strength material to the extreme tension fibers of the existing structure. Both buildings and bridges have been repaired via this technique, with either steel plates or fiber reinforced composite (FRC) laminates employed as

* Tel.: +44-117-928-9735; fax: +44-117-928-7783.
*E-mail address:* wendel.sebastian@bristol.ac.uk (W.M. Sebastian).

0020-7683/02/$ - see front matter © 2002 Published by Elsevier Science Ltd.
PII: S0020-7683(02)00516-4

the additional tension-resisting reinforcement. FRC laminates are gaining strong popularity owing to their enhanced stiffness, strength, fatigue, corrosion-resistance, reduced weight, ease of installation and consequent minimization of disruption to the function of the structure during this installation. To date, mainly concrete structures have been enhanced via this technique, but there is an increasing realization within the structural rehabilitation industry that a large inventory of metallic structures may also benefit from this technology. This paper considers the specific application of the technology to I-section steel beams.

In any steel–FRC or concrete–FRC member, the development of hybrid structural action is strongly reliant on the successful transfer of stresses between the FRC laminate and the original steel or concrete beam. Since these stresses are transferred via shearing action of the bonding adhesive layer, the shear-bond stresses developed in the adhesive play an important role in the structural responses of such hybrid members to external loads. If these shear-bond stresses exceed the strength of the weakest of the materials (adhesive, FRC, steel or concrete) at the joint, then material failure occurs locally and hybrid structural action is compromised. It is well known that in FRC-laminated concrete members, such high shear-bond stresses trigger brittle fracture of the concrete and eventually lead to complete separation of the FRC laminate from the original member. Various separation modes have been investigated, via experiment and analysis, by researchers including Malek et al. (1998), Triantafillou and Plevris (1992), Täljsten (1994), Sebastian (2001), and Kim and Sebastian (2002). These studies show that initiation and propagation of brittle separation in FRC-laminated concrete members is influenced by vertical and inclined cracks in the concrete. A comprehensive summary of research on, and practical applications of, FRC laminating technology in concrete structures to date is given by Hollaway and Leeming (1999).

Research into the performance of FRC-laminated steel beams under external loading is in progress at the University of Bristol. This work shows that such members can also fail by separation of the laminate from the beam, due to the influence of high shear-bond stresses. The failure has been observed to initiate at either of two locations, namely the elastic–plastic (maximum moment) zone of the hybrid member once yielding of the steel is well underway, or the fully elastic region near the ends of the laminate. Roberts (1989) has given a thorough predictive analysis of the shear-bond stresses associated with separation failure starting near the ends of the laminate. This analysis was applied (Roberts, 1989) to uncracked FRC-laminated concrete beams, so it is equally valid for FRC-laminated steel beams. Hence analysis of these laminate-end shear-bond stresses is not pursued further in this paper. However, to date, no models have been presented to predict the magnitudes of the shear-bond stresses which initiate separation failure in elastic–plastic zones of FRC-laminated steel beams. This situation has provided the motivation for the present work.

In the next section, some physical insight is given into the mechanics of shear-bond stress development within elastic–plastic zones of FRC-laminated steel members. This insight is used to explain how the well-known linear dependency of shear-bond stress on shear force may be expected to change during elastic–plastic behavior. It is also used to explain the need for two-parameter models, as well as the need to consider five phases of behavior, for success in predicting shear-bond stresses developed during the elastic–plastic regime. Next, predictive algebraic models are presented for the shear-bond stresses associated with each of these five elastic–plastic phases, and predictions from the models are compared with finite element (FE) predictions and with test data. The capabilities of the models are then discussed and conclusions are drawn.

## 2. Development of predictive models

### *2.1. Mechanics of shear-bond stress development*

Fig. 1(a)–(c) shows, respectively, a steel I-section–adhesive–FRC laminate hybrid member in elevation and in section, and a free body diagram of an infinitesimal element of the laminate along the length of the member. Equilibrium of the element of laminate and the FRC material axial constitutive relation gives:

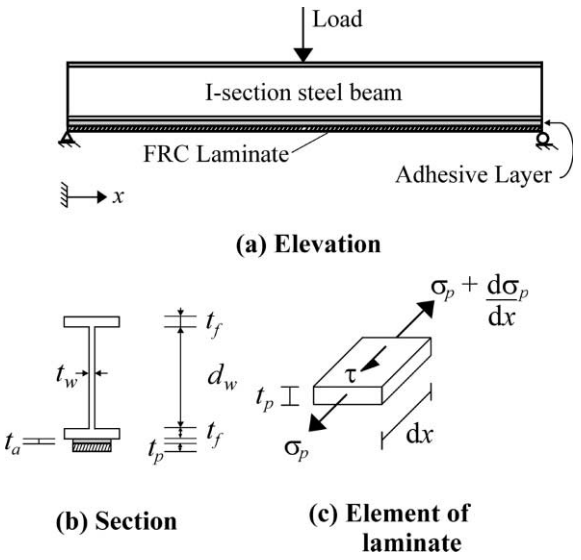


Fig. 1. I-section steel beam with adhesively bonded FRC laminate.

$$\tau = t_{\mathrm{p}} \frac{\mathrm{d}(\sigma_{\mathrm{p}})}{\mathrm{d}x} = t_{\mathrm{p}} E_{\mathrm{p}} \frac{\mathrm{d}(\varepsilon_{\mathrm{p}})}{\mathrm{d}x}, \tag{1}$$

where $\tau$ is the shear-bond stress, $t_{\mathrm{p}}$ and $E_{\mathrm{p}}$ are the thickness and Young's Modulus of the laminate, $\sigma_{\mathrm{p}}$ and $\varepsilon_{\mathrm{p}}$ are the axial stress and axial strain at the mid-thickness of the laminate (assuming a linear distribution of axial strain through the thickness of the laminate), and $x$ is distance along the beam. Note that FRC materials remain linearly elastic up to rupture. Eq. (1) clearly states that the shear-bond stress is directly proportional to the longitudinal gradient of the axial strain at the mid-thickness of the laminate. Hence the variation in slope of an $\varepsilon_{\mathrm{p}}$-versus-$x$ plot will give a direct measure of the variation of shear-bond stress along the beam. This idea will be repeatedly exploited further on in the present paper to help development various arguments.

During fully elastic behavior the hybrid member is stiff, so curvature changes, and hence axial strain changes along the FRC laminate, are low under the influence of bending moments induced by external loads. However, in elastic–plastic zones, only the FRC laminate and the progressively shrinking core of elastic steel can resist further moments, so member stiffness is low. This causes the rate of increase, with additional moment, of section curvature (and hence of laminate strain) to rise dramatically. Hence the strain gradients along the laminate increase significantly in progressing from fully elastic zones to elastic–plastic zones of FRC-laminated I-section steel beams. Since the shear-bond stress is directly proportional to the strain gradient in the laminate, it is easy to see why shear-bond stresses also increase sharply from elastic to partially plastic zones of these hybrid members.

### 2.2. Why two-parameter models and why does the neutral axis move?

In Fig. 1, consider the original I-section steel beam without the bonded FRC laminate. From symmetry, it is clear that whether the section is fully elastic or elastic–plastic, the neutral axis for flexure in a vertical plane is located at mid-depth. Hence the neutral axis can be located from symmetry considerations only. This means that during elastic–plastic flexure, only one parameter, namely that which defines the distance from the neutral axis to the inner boundary of the plastic zone, is required to fully define section behavior.

However, once the FRC laminate is bonded and causes the tension flange to grow, the section becomes vertically asymmetric and so the above arguments are no longer valid. For this reason, two parameters are required to fully define the behavior of the steel–FRC hybrid section during the elastic–plastic regime; one parameter to locate the neutral axis, and the other to define the extent of plastification of the section. Note that this argument assumes rigid bond between the FRC laminate and the steel I-section. In practice, the adhesive layer is of finite shear stiffness. The implications of the disparity between the rigid bond assumption and the reality of a shear-flexible adhesive connection will evolve during the discussions further on in this paper.

During fully elastic behavior, the height of the neutral axis remains fixed. This is because, assuming a fixed height of neutral axis, the axial stresses alter by the same proportion down the entire depth of the section as curvature increases within the elastic regime, and so the zero axial force condition on any section can be maintained irrespective of the magnitude of the moment acting on the section. However as the curvature of the hybrid section increases during the elastic–plastic regime of behavior, the axial strain, and hence the axial stress (because the laminate is linearly elastic up to rupture), in the FRC laminate increase significantly, while the stresses on the compression side of the neutral axis can increase only up to a maximum of the yield stress of the steel. Due to this progressively high increase in stress on the tension side and a contrastingly low increase in average stress on the compression side of the neutral axis, the only means by which the zero axial force condition on the section can be maintained is for the zone of compressive stress to expand relative to the zone of tensile stress. In other words, as section curvature increases during elastic–plastic behavior, the neutral axis must shift progressively towards the tension flange. Immobilization of the elastic–plastic neutral axis by bonding an equal area of FRC laminate to the compression flange may not be realizable in practice, owing to the strong potential for buckling of this new (thin) laminate at low compressive stress.

The standard beam-theory expression for shear-bond stress is $VA_p y_p / I_t b_p$, where $V$ is the shear force on the section, $A_p$ is the area of the laminate, $y_p$ is the distance from the neutral axis of the hybrid section to the mid-thickness of the laminate, $I_t$ is the transformed second moment of area of the entire hybrid section in FRC units, and $b_p$ is the width of the laminate. The derivation of this expression assumes that both the material properties and the height of the neutral axis are fixed along the beam. From the arguments of the preceding paragraphs, it is clear that neither of these assumptions holds true in moment-varying elastic–plastic regions of FRC-laminated I-section steel beams. The complex behavior introduced by neutral axis shift and by progressive plastification of the steel must be allowed for in any modeling of elastic–plastic shear-bond stresses. In the next section, the different phases of elastic–plastic behavior to be considered for such modeling are identified.

### 2.3. The five phases of elastic–plastic behavior

Since the width of the FRC–steel hybrid section is not constant throughout its depth, the equations of axial and moment equilibrium change as plastification progresses on from the flanges to the webs of the steel I-section. This leads to five possible phases of elastic–plastic behavior, all of which are shown in Fig. 2, and each of which must be considered individually. As explained previously, each phase is defined completely by two parameters, namely the vertical location of the neutral axis, and the extent of plastification of the section. Hence, in Fig. 2, a through-depth axial strain distribution is given to permit location of the neutral axis, while the yielded regions of steel are shaded to indicate the extent of plastification. In progressing from phase 1 to phase 5, section curvature increases monotonically and the neutral axis shifts unidirectionally towards the FRC laminate.

Yielding of the section first occurs at the extreme steel compression fiber, since that is the steel fiber furthest away from the elastic neutral axis. Afterwards, plasticity progresses through the compression flange (phase 1), compression web (phase 2), tension flange (phase 3), tension web (phase 4), and then back

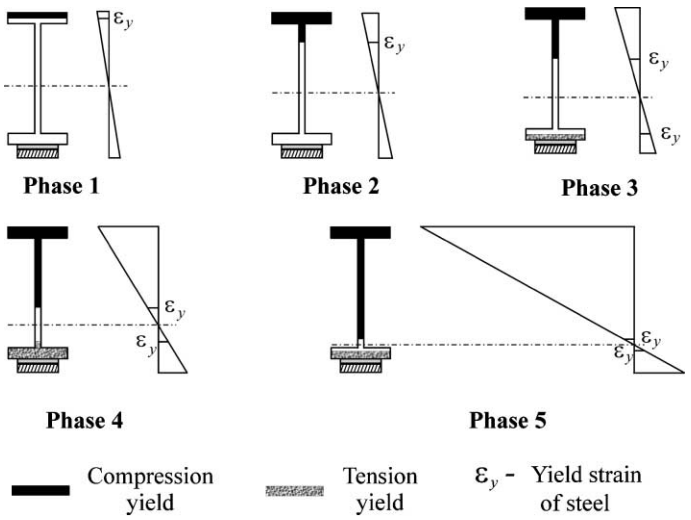


Fig. 2. Phases of elastic–plastic behavior.

into the tension flange (phase 5). Note that if the area of the FRC laminate is small, yielding of the tension flange may initiate before that of the compression web. However, in practice, the areas of laminate required from moment capacity-increase or member stiffness-increase considerations will typically exceed these small values, so the progression of plasticity depicted in Fig. 2 will frequently occur. Note also that, after initiation of phase 4, incremental plastification of the tension web initially occurs away from the FRC laminate up to a maximum distance, then back towards the laminate, first down the web (still phase 4) and then back into the (steel) tension flange (phase 5). During phases 4 and 5, the section neutral axis remains confined to the web. Beyond phase 5, the neutral axis may progress even further towards the FRC laminate and eventually penetrate the partially tensioned flange. However, it is unlikely that this will occur in practice, since the large strains which develop in the vicinity of the extreme compression fibers as the neutral axis moves in close proximity to the laminate may well induce buckling of the compression flange and/or web beforehand. Thus elastic–plastic phases beyond phase 5 are not considered for modeling in this paper.

It is important to note that, mathematically, phases 3 and 5 are identical. Hence one set of expressions should suffice to define both these phases. This reduces the required algebraic effort from five to four different models. This mathematical synonymity of phases 3 and 5 is exploited in the following section, where four mathematical models are presented to describe phases 1–5.

### 2.4. The mathematical models

The models presented here assume a shear-rigid adhesive layer. The implications of the disparity between this assumption and the reality of a shear-deformable adhesive layer will emerge when the model predictions are compared with FE predictions and with laboratory test data later in this paper. It is also assumed that any shear stresses within the steel are small and so have a negligible effect on yielding of the steel. Hence plastification of steel is assumed to occur when the axial stress in the steel equals the uniaxial yield stress. This also implies a linear through-depth distribution of axial strains in the steel.

For the hybrid section shown in Fig. 1(b), each steel flange is of area $A_f$ and thickness $t_f$, the steel web is of thickness $t_w$ and depth $d_w$, while the FRC laminate is of thickness $t_p$. The steel is of Young's modulus $E_s$ and yield stress $\sigma_y$, while the FRC is of Young's modulus $E_p$. In all mathematical analyses given henceforth,

the presence of a dot above a parameter is used to denote differentiation of that parameter with respect to distance ($x$) along the hybrid member (Fig. 1(a)). The following quantities appear in the modeling of all five phases of elastic–plastic behavior, so it is convenient to define them here, as follows:

$$T = t_f + t_a + t_p/2; \quad T_1 = t_f + t_a; \quad T_2 = t_f + t_a + 2t_p/3; \quad T_3 = T + T_1. \tag{2a–d}$$

*2.4.1. Phase 1*

This phase is defined by the progression of plasticity through the compression flange only. The two parameters, $\alpha$ and $\beta$, chosen to define this phase are shown in Fig. 3. The depth of web in compression is $\alpha d_w$, while the depth of elastic compression flange is $\beta t_f$. In order that yielding of the steel remains confined to the compression flange, the following inequalities must be satisfied by $\alpha$ and $\beta$:

$$1 \geqslant \beta \geqslant 0 \quad \text{and} \quad (1-\alpha)d_w + t_f \leqslant \alpha d_w + \beta t_f \Rightarrow (1-\beta)t_f \leqslant d_w(2\alpha - 1). \tag{3a–c}$$

From the linear through-depth strain and rigid bond assumptions, the axial strain ($\varepsilon_p$) at the mid-thickness of the laminate is as follows:

$$\varepsilon_p = \frac{\sigma_y}{E_s}\frac{((1-\alpha)d_w + T)}{(\alpha d_w + \beta t_f)}. \tag{4}$$

From Eqs. (1) and (4), the expression for shear-bond stress during phase 1 is:

$$\tau = t_p E_p \frac{d(\varepsilon_p)}{dx} = \frac{t_p E_p \sigma_y}{E_s}\frac{d\left(\frac{((1-\alpha)d_w+T)}{(\alpha d_w+\beta t_f)}\right)}{dx} = -\frac{t_p E_p \sigma_y}{E_s}\frac{((\alpha d_w + \beta t_f)d_w + (d_w + \phi t_f)((1-\alpha)d_w + T))}{(\alpha d_w + \beta t_f)^2}\dot{\alpha}, \tag{5}$$

where, as explained previously, a dot over a parameter denotes differentiation with respect to distance ($x$) along the beam, and where the quantity $\phi$ is defined as follows:

$$\phi = \frac{\dot{\beta}}{\dot{\alpha}}. \tag{6}$$

It is clear from Eq. (5) that, for a given value of $\beta$, the shear-bond stress can be determined only if the corresponding values of $\alpha$, $\phi$ and $\dot{\alpha}$ are also known. The parameter $\alpha$ is determined from the following equation expressing the condition of zero net axial force on the section:

$$\begin{aligned}(1-\beta)A_f + \frac{(\alpha d_w + \beta t_f/2)}{(\alpha d_w + \beta t_f)}\beta A_f + \frac{b_w(\alpha d_w)^2}{2(\alpha d_w + \beta t_f)} \\ = \frac{b_w((1-\alpha)d_w)^2}{2(\alpha d_w + \beta t_f)} + \frac{((1-\alpha)d_w + t_f/2)}{(\alpha d_w + \beta t_f)}A_f + \frac{((1-\alpha)d_w + T)}{(\alpha d_w + \beta t_f)}\frac{A_p E_p}{E_s}.\end{aligned} \tag{7}$$

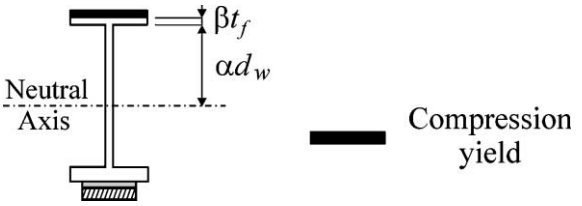


Fig. 3. Definition of parameters for phase 1.

Solution of this equation for $\alpha$ is simplified by manipulation into the following form:

$$\alpha = \left( \frac{2(T + d_w)E_pA_p + E_s(d_w(2A_f + b_w d_w) + A_f t_f(\beta^2 - 2\beta + 1))}{2d_w(E_s(2A_f + b_w d_w) + E_pA_p)} \right). \tag{8}$$

In order to find an expression for $\phi$, it is convenient to rewrite Eq. (7) as follows:

$$\beta^2 - 2\beta + 1 = \frac{(2\alpha - 1)d_w(2A_f + b_w d_w) + 2((\alpha - 1)d_w - T)E_pA_p/E_s}{A_f t_f}. \tag{9}$$

Differential calculus may then be applied to Eq. (9) to give $\phi$ as follows:

$$\phi = \frac{d_w(E_s(2A_f + b_w d_w) + E_pA_p)}{E_s A_f t_f(\beta - 1)}. \tag{10}$$

The parameter $\dot{\alpha}$ is found by first considering the following equation of moment equilibrium:

$$M_{tot} = M_{cf} + M_w + M_{tf} + M_p, \tag{11}$$

where $M_{tot}$ is the total moment on the section, and where $M_{cf}$, $M_w$, $M_{tf}$ and $M_p$ are, respectively, the moment contributions from the compression flange, entire web, tension flange and FRC laminate. Expressions for these moment contributions are as follows:

$$\frac{M_{cf}}{\sigma_y} = A_f \left( (1 - \beta)(\alpha d_w + 0.5(1 + \beta)t_f) + \frac{\beta(2\alpha d_w(\alpha d_w + 0.5\beta t_f) + \beta t_f(\alpha d_w + 2\beta t_f/3))}{2(\alpha d_w + \beta t_f)} \right), \tag{12}$$

$$\frac{M_w}{\sigma_y} = \frac{(\alpha^3 + (1 - \alpha)^3)b_w d_w^3}{3(\alpha d_w + \beta t_f)}, \tag{13}$$

$$\frac{M_{tf}}{\sigma_y} = A_f \left( \frac{2d_w(1 - \alpha)((1 - \alpha)d_w + 0.5t_f) + t_f((1 - \alpha)d_w + 2t_f/3)}{2(\alpha d_w + \beta t_f)} \right), \tag{14}$$

$$\frac{M_p}{\sigma_y} = \frac{E_pA_p}{E_s} \left( \frac{2((1 - \alpha)d_w + T)((1 - \alpha)d_w + T_1) + t_p((1 - \alpha)d_w + T_2)}{2(\alpha d_w + \beta t_f)} \right), \tag{15}$$

where $T$, $T_1$ and $T_2$ are as defined in Eqs. (2a–c). By combining Eqs. (11)–(15), differentiating the result and simplifying, an expression for $\dot{\alpha}$ may be found as follows:

$$\dot{\alpha} = \frac{2V(\alpha d_w + \beta t_f)}{\sigma_y \psi_1}, \tag{16}$$

where $V$ is the shear force at the section concerned, and $\psi_1$ is given by the following expression:

$$\begin{aligned} \psi_1 = {} & A_f(2(\alpha d_w + 0.5(1 + \beta)t_f)((1 - \beta)(d_w + \phi t_f) - \phi(\alpha d_w + \beta t_f)) + 2(d_w + 0.5\phi t_f)(\alpha d_w + \beta t_f(1 - \beta)) \\ & + 2d_w(\alpha d_w + 0.5\beta t_f)(\alpha\phi + \beta) + \beta t_f(\beta(d_w + 2\phi t_f/3) + 2\phi(\alpha d_w + 2\beta t_f/3)) - 2d_w(2d_w(1 - \alpha) + t_f)) \\ & + 2(2\alpha - 1)b_w d_w^3 - \frac{E_pA_p d_w}{E_s}(2(2d_w(1 - \alpha) + T_3) + t_p) - 2M_{tot}(d_w + \phi t_f)/\sigma_y, \end{aligned} \tag{17}$$

where $T_3$ is as defined in Eq. (2d).

Note that once the total moment on the section is found by combining Eqs. (11)–(15), the moment diagram for the hybrid member under the given external loading must be consulted to determine the location along the member at which that moment acts. Once this location is known, the shear force required in Eq. (16) is taken as the value on the associated shear force diagram (also for the given external loading) at that location. Hence by considering a few values of $\alpha$ and $\beta$ within the limits defined by Eq. (3), and by

applying the appropriate expressions from Eqs. (5)–(17), the variation of shear-bond stress corresponding to phase 1 of elastic–plastic behavior in an FRC-laminated I-section steel beam under any pattern of loading may be fully determined.

*2.4.2. Phase 2*

In this phase, plasticity occurs within the entire compression flange and through part of the compression web only. The two parameters $\alpha$ and $\beta$ are again used. As shown in Fig. 4, the parameters are now defined such that the depth of web in tension is $\alpha d_w$, while the depth of elastic compression web is $\beta d_w$. For yield to be present in the compression web and absent from the tension flange, the relationship between parameters $\alpha$ and $\beta$ must lie within limits defined as follows:

$$\alpha + \beta \leqslant 1 \quad \text{and} \quad \alpha d_w + t_f \leqslant \beta d_w \Rightarrow \beta - \alpha \geqslant t_f/d_w. \tag{18a–c}$$

The derivation proceeds along the same broad lines as in the previous section for phase 1. First, the axial strain ($\varepsilon_p$) at the mid-thickness of the laminate is given as follows:

$$\varepsilon_p = \frac{\sigma_y}{E_s}\frac{(\alpha d_w + T)}{\beta d_w}. \tag{19}$$

From Eqs. (1) and (19), the shear-bond stress during phase 2 is:

$$\tau = t_p E_p \frac{d(\varepsilon_p)}{dx} = \frac{t_p E_p \sigma_y}{E_s}\frac{d\left(\frac{(\alpha d_w + T)}{\beta d_w}\right)}{dx} = \frac{t_p E_p \sigma_y}{E_s}\frac{(\beta d_w - \phi(\alpha d_w + T))}{d_w \beta^2}\dot{\alpha}, \tag{20}$$

where the parameter $\phi$ is as defined in Eq. (6), and other parameters are as defined above.

For a given value of $\alpha$, the corresponding value of $\beta$ is determined from the following equation expressing the condition of zero net axial force on the section:

$$A_f\left(1 - \frac{(\alpha d_w + t_f/2)}{\beta d_w}\right) + b_w d_w\left((1 - \beta - \alpha) + \frac{(\beta + \alpha)(\beta - \alpha)}{2\beta}\right) = \frac{A_p E_p}{E_s}\frac{(\alpha d_w + T)}{\beta d_w} \tag{21}$$

which, on simplification, gives the following quadratic in $\beta$:

$$\beta^2 + \frac{2(b_w d_w(\alpha - 1) - A_f)}{b_w d_w}\beta + \frac{\alpha d_w(2A_f + \alpha b_w d_w) + 2A_p E_p/E_s(\alpha d_w + T) + A_f t_f}{b_w d_w^2} = 0. \tag{22}$$

Eq. (22) may now be differentiated to give the following expression for $\phi$:

$$\phi = \frac{(b_w d_w(\beta + \alpha) + A_f + E_p A_p/E_s)}{A_f + b_w d_w(1 - \alpha - \beta)}. \tag{23}$$

The parameter $\dot{\alpha}$ is then found by first considering the following moment equation:

$$M_{tot} = M_{ctf} + M_w + M_p, \tag{24}$$

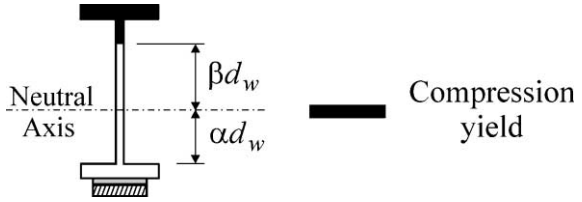


Fig. 4. Definition of parameters for phase 2.

where $M_{tot}$ is the total moment on the section, and where $M_{ctf}$, $M_w$ and $M_p$ are the moment contributions from the compression and tension flanges together, from the entire web, and from the FRC laminate, respectively. Expressions for these moment contributions are as follows:

$$\frac{M_{ctf}}{\sigma_y} = A_f\left(((1-\alpha)d_w + 0.5t_f) + \frac{\alpha}{\beta}(\alpha d_w + 0.5t_f) + \frac{t_f}{2\beta d_w}(\alpha d_w + 2t_f/3)\right), \tag{25}$$

$$\frac{M_w}{\sigma_y} = b_w d_w^2\left(\frac{\alpha^3}{3\beta} + \frac{\beta^2}{3} + (1-\alpha-\beta)\frac{(1-\alpha+\beta)}{2}\right) = b_w d_w^2\frac{(2\alpha^3 - \beta^3 + 3\beta(1-\alpha)^2)}{6\beta}, \tag{26}$$

$$\frac{M_p}{\sigma_y} = \frac{E_p A_p}{E_s}\left(\frac{2(\alpha d_w + T)(\alpha d_w + T_1) + t_p(\alpha d_w + T_2)}{2\beta d_w}\right), \tag{27}$$

where $T$, $T_1$ and $T_2$ are as defined in Eqs. (2a–c). By combining Eqs. (24)–(27), differentiating and simplifying, the following expression for $\dot{\alpha}$ results:

$$\dot{\alpha} = \frac{2\beta d_w V}{\sigma_y \psi_2}, \tag{28}$$

where $V$ is the shear force on the section and $\psi_2$ is as follows:

$$\psi_2 = 2A_f d_w(\phi((1-\alpha)d_w + 0.5t_f) + d_w(2\alpha - \beta) + t_f) + (2\alpha^2 + \phi((1-\alpha)^2 - \beta^2) - 2\beta(1-\alpha))b_w d_w^3 + \frac{E_p A_p d_w}{E_s}(2(2\alpha d_w + T_3) + t_p) - 2\phi d_w M_{tot}/\sigma_y, \tag{29}$$

where $T_3$ is as defined in Eq. (2d). Note that the lowest value of $\beta$ considered for phase 2 calculations should equal the highest value of $\alpha$ used for phase 1 calculations. This corresponds to the coincidence of phases 1 and 2, when plastification just occurs at the compression web–compression flange junction.

### 2.4.3. Phases 3 and 5

In both these phases, plasticity occurs within the entire compression flange, in part of the compression web, and in part of the tension flange. The two parameters $\alpha$ and $\beta$, defined as in Fig. 5, are such that the depth of web in tension is $\alpha d_w$, while the depth of elastic tension flange is $\beta t_f$. To ensure no yield in the tension web, and also to ensure yield in the compression web, $\alpha$ and $\beta$ must relate to each other within the following limits:

$$1 \geqslant \beta \geqslant 0 \quad \text{and} \quad \alpha d_w + \beta t_f \leqslant (1-\alpha)d_w \Rightarrow \beta t_f \leqslant (1-2\alpha)d_w. \tag{30a–c}$$

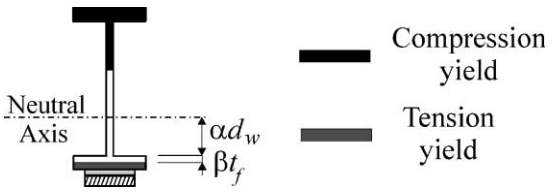


Fig. 5. Definition of parameters for phases 3 and 5.

The axial strain ($\varepsilon_p$) at the mid-thickness of the laminate is given as follows:

$$\varepsilon_p = \frac{\sigma_y}{E_s}\frac{(\alpha d_w + T)}{(\alpha d_w + \beta t_f)}. \tag{31}$$

From Eqs. (1) and (31), the shear-bond stress during phases 3 and 5 is:

$$\tau = t_p E_p \frac{d(\varepsilon_p)}{dx} = \frac{t_p E_p \sigma_y}{E_s}\frac{d\left(\frac{(\alpha d_w + T)}{(\alpha d_w + \beta t_f)}\right)}{dx} = \frac{t_p E_p \sigma_y}{E_s}\frac{((\alpha d_w + \beta t_f)d_w - (d_w + \phi t_f)(\alpha d_w + T))}{(\alpha d_w + \beta t_f)^2}\dot{\alpha}, \tag{32}$$

where $\phi$ is defined in Eq. (6), and other parameters are as defined above.

For a given value of $\beta$, the corresponding value of $\alpha$ is determined from the following equation expressing the condition of zero net axial force on the section:

$$\begin{aligned} &A_f\left(1-(1-\beta)-\left(\frac{\alpha d_w + \beta t_f/2}{\alpha d_w + \beta t_f}\right)\beta\right) + b_w(d_w(1-2\alpha)-\beta t_f) + \left(\frac{\alpha d_w + \beta t_f/2}{\alpha d_w + \beta t_f}\right) b_w \beta t_f \\ &\quad = \left(\frac{\alpha d_w + T}{\alpha d_w + \beta t_f}\right)\frac{A_p E_p}{E_s} \end{aligned} \tag{33}$$

which, on simplification, gives the following quadratic in $\alpha$:

$$2b_w d_w^2 \alpha^2 + d_w(b_w(2\beta t_f - d_w) + A_p E_p/E_s)\alpha + \frac{t_f(b_w t_f - A_f)}{2}\beta^2 - b_w t_f d_w \beta + \frac{A_p E_p T}{E_s} = 0. \tag{34}$$

Eq. (34) may be differentiated to give the following expression for $\phi$:

$$\phi = \frac{d_w(E_s b_w(2\beta t_f + d_w(4\alpha - 1)) + E_p A_p)}{E_s t_f(\beta(A_f - b_w t_f) + b_w d_w(1-2\alpha))}. \tag{35}$$

The parameter $\dot{\alpha}$ is then found by first considering the following moment equation:

$$M_{tot} = M_{ctf} + M_w + M_p, \tag{36}$$

where all parameters of Eq. (36) are as defined immediately after Eq. (24). Expressions for $M_{ctf}$, $M_w$ and $M_p$ are as follows:

$$\begin{aligned} \frac{M_{ctf}}{\sigma_y} = A_f\Bigg(&((1-\alpha)d_w + 0.5t_f) + (1-\beta)(\alpha d_w + 0.5(1+\beta)t_f) + \frac{\alpha d_w}{(\alpha d_w + \beta t_f)}\beta(\alpha d_w + 0.5\beta t_f) \\ &+ \frac{\beta t_f}{2(\alpha d_w + \beta t_f)}\beta(\alpha d_w + 2\beta t_f/3)\Bigg), \end{aligned} \tag{37}$$

$$\frac{M_w}{\sigma_y} = b_w(d_w(1-2\alpha) - \beta t_f)\frac{(d_w + \beta t_f)}{2} + \frac{b_w}{3}(\alpha d_w + \beta t_f)^2 + \frac{b_w(\alpha d_w)^3}{3(\alpha d_w + \beta t_f)}, \tag{38}$$

$$\frac{M_p}{\sigma_y} = \frac{E_p A_p}{E_s}\left(\frac{2(\alpha d_w + T)(\alpha d_w + T_1) + t_p(\alpha d_w + T_2)}{2(\alpha d_w + \beta t_f)}\right), \tag{39}$$

where $T$, $T_1$ and $T_2$ are as defined in Eqs. (2a–c). By combining Eqs. (36)–(39), differentiating and simplifying, the following expression for $\dot{\alpha}$ results:

$$\dot{\alpha} = \frac{2V(\alpha d_w + \beta t_f)}{\sigma_y \psi_3}, \tag{40}$$

where $V$ is the shear force on the section and $\psi_3$ is as follows:

$$\psi_3 = A_f(2(d_w + t_f)(d_w + \phi t_f) - \beta t_f(\beta\phi t_f + d_w(2\alpha\phi + \beta))) + ((\alpha d_w + \beta t_f)(\phi t_f(d_w + \beta t_f) + d_w((2\alpha - 1)d_w + \beta t_f)) + (d_w + \beta t_f)(d_w + \phi t_f)(d_w(1 - 3\alpha) - 2\beta t_f) + 2\alpha^2 d_w^3)b_w + \frac{E_p A_p d_w}{E_s}(2(2\alpha d_w + T_3) + t_p) - 2M_{tot}(d_w + \phi t_f)/\sigma_y, \quad (41)$$

where $T_3$ is as defined in Eq. (2d).

Frequently, phase 5 ends with the section neutral axis at the tension flange–web junction. If this corresponds to a value of $\beta$ equal to $\beta_1$, then for all values of $\beta$ less than or equal to $\beta_1$, Eq. (34) gives two positive values of $\alpha$ both less than 1.0. The higher and lower values will correspond to phases 3 and 5 respectively. For values of $\beta$ exceeding $\beta_1$, only one positive value of $\alpha$ will exist, and that value will define phase 3 behavior. Occasionally, phase 5 may also end with the neutral axis away from the web–flange junction, with yield of only the extreme tension steel fiber in the tension zone.

### 2.4.4. Phase 4

For this phase, characterized by yield of both tension and compression flanges and webs, parameters $\alpha$ and $\beta$ define, respectively, the total depth of web in tension ($\alpha d_w$) and the depth of elastic tension web ($\beta d_w$), as shown in Fig. 6. These definitions are satisfied provided that:

$$\beta \leqslant \alpha \quad \text{and} \quad \alpha d_w + \beta d_w \leqslant d_w \Rightarrow \alpha + \beta \leqslant 1. \quad (42a\text{–}c)$$

The axial strain ($\varepsilon_p$) at the mid-thickness of the laminate is given as follows:

$$\varepsilon_p = \frac{\sigma_y}{E_s}\frac{(\alpha d_w + T)}{\beta d_w}. \quad (43)$$

From Eqs. (1) and (43), the shear-bond stress during phase 4 is:

$$\tau = t_p E_p \frac{d(\varepsilon_p)}{dx} = \frac{t_p E_p \sigma_y}{E_s}\frac{d\left(\frac{(\alpha d_w + T)}{\beta d_w}\right)}{dx} = \frac{t_p E_p \sigma_y}{E_s d_w}\frac{(\beta d_w - \phi(\alpha d_w + T))}{\beta^2}\dot{\alpha}, \quad (44)$$

where $\phi$ is defined in Eq. (6), and other parameters are as defined above.

For a given value of $\alpha$, the determination of $\beta$ from the axial force equilibrium expression is as follows:

$$(1 - 2\alpha)b_w d_w = \frac{A_p E_p}{E_s}\frac{(\alpha d_w + T)}{\beta d_w} \Rightarrow \beta = \frac{A_p E_p}{E_s}\frac{(\alpha d_w + T)}{(1 - 2\alpha)b_w d_w^2}. \quad (45a, b)$$

Differentiation of Eq. (45b) gives $\phi$ as:

$$\phi = \frac{(2\beta E_s b_w d_w + E_p A_p)}{E_s b_w d_w (1 - 2\alpha)}. \quad (46)$$

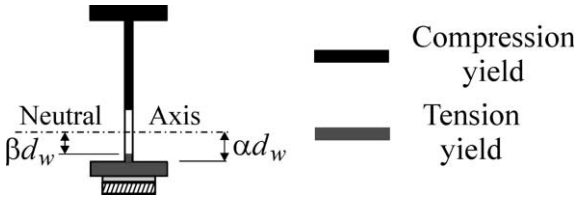


Fig. 6. Definition of parameters for phase 4.

As previously, $\dot{\alpha}$ is found by first considering the following moment equation:

$$M_{\text{tot}} = M_{\text{ctf}} + M_{\text{w}} + M_{\text{p}}, \tag{47}$$

where $M_{\text{ctf}}$, $M_{\text{w}}$ and $M_{\text{p}}$, all defined immediately after Eq. (24), are as follows:

$$\frac{M_{\text{ctf}}}{\sigma_{\text{y}}} = A_{\text{f}}(d_{\text{w}} + t_{\text{f}}), \tag{48}$$

$$\frac{M_{\text{w}}}{\sigma_{\text{y}}} = \frac{(6\alpha(\alpha-1)+3-2\beta^2)b_{\text{w}}d_{\text{w}}^2}{6}, \tag{49}$$

$$\frac{M_{\text{p}}}{\sigma_{\text{y}}} = \frac{E_{\text{p}}A_{\text{p}}}{E_{\text{s}}}\left(\frac{2(\alpha d_{\text{w}}+T)(\alpha d_{\text{w}}+T_1)+t_{\text{p}}(\alpha d_{\text{w}}+T_2)}{2\beta d_{\text{w}}}\right). \tag{50}$$

Combination and differentiation of Eqs. (47)–(50) give $\dot{\alpha}$ as:

$$\dot{\alpha} = \frac{2\beta d_{\text{w}}V}{\sigma_{\text{y}}\psi_4}, \tag{51}$$

where $V$ is the shear force on the section and $\psi_4$ is as follows:

$$\psi_4 = 2\phi d_{\text{w}}A_{\text{f}}(d_{\text{w}}+t_{\text{f}}) + (2(\alpha\beta+(\alpha-1)(\beta+\alpha\phi)) + \phi(1-2\beta^2))b_{\text{w}}d_{\text{w}}^3 + \frac{E_{\text{p}}A_{\text{p}}d_{\text{w}}}{E_{\text{s}}}(2(2\alpha d_{\text{w}}+T_3)+t_{\text{p}}) - 2\phi d_{\text{w}}M_{\text{tot}}/\sigma_{\text{y}}. \tag{52}$$

It is envisaged that, for economy, either phase 5 or phase 4 will commonly be used to define the ultimate limit state in many practical designs.

*2.4.5. Nonlinearity of shear stress–shear force relationship*

A scrutiny of the mathematical analyses given in Sections 2.4.1–2.4.4 shows that the shear-bond stress is nonlinearly proportional to the corresponding shear force. For phase 1, this is demonstrated by noting the dependency of the shear-bond stress on the parameter $\dot{\alpha}$ in Eq. (5), followed by the proportionality of $\dot{\alpha}$ to the shear force ($V$) in Eq. (16) via parameters (such as $\psi_1$) which are all highly nonlinear functions (Eqs. (8), (10) and (17)) of their constituent variables. This is in sharp contrast to the elastic relationship, when shear-bond stress is directly proportional to shear force.

For a load generating elastic–plastic behavior in the hybrid member, some or all of the above five elastic–plastic phases will occur in different zones along the member. The actual number of phases present will depend on the maximum moment in the member. In all cases, the elastic–plastic section of lowest moment will be defined by phase 1 with a value of $\beta$ equal to 1.0 in Eqs. (4)–(17). If several phases are present, these phases will occur in the order phase 1, 2, 3 and so on, each over a short length, as the hybrid member is traversed in the direction of increasing moment. This and other ideas have been demonstrated in an extensive numerical study conducted to establish the degree of validity of the above algebraic models. The results of that study are presented in the next section.

## 3. Verification study

In this verification study, both the axial strains in the FRC laminate and the shear-bond stresses in the adhesive layer as predicted by the present algebraic models are compared with corresponding data from a nonlinear FE program and from laboratory testing. In the remainder of this section, the salient features of

the FE program are discussed, the hybrid members used for the verification study are described, and the data comparisons are made.

### 3.1. Brief description of finite element computer program

The FE program used here has been developed for the analysis of general hybrid structures of different materials joined by shear connectors. This program has been used (Sebastian and McConnel, 2000) to successfully analyse different forms of hybrid structure, including solid reinforced concrete slabs, classical steel I-section–stud shear connector–solid concrete slab hybrid members, and steel space truss–stud shear connector–ribbed concrete slab–profiled steel decking hybrid bridges. In all cases, detailed modeling of the flexible shear connectors was performed. Slip through, and the failure sequences of, the shear connectors as predicted by the program compared well with laboratory data. The present steel I-section–adhesive–FRC laminate member, in which the continuum adhesive layer serves the roles of the shear connector, is yet another form of hybrid structure to which the FE program is being applied.

Fig. 7 shows the typical assembly of elements used in the program to model the present steel–FRC hybrid structural form. As can be seen, a two-noded bending-membrane element models each of the laminate and the steel beam, while a specialized coupling element models the adhesive. Each bending-membrane element is layered to permit modeling of the through-depth variation of material properties due to progressive spatial plastification of the steel. Each coupling element, which represents a volume of adhesive halfway between itself and its nearest neighbors, comprises three springs. The shear spring of Fig. 7(b) permits relative horizontal movement between the laminate and the steel member, and so represents slip

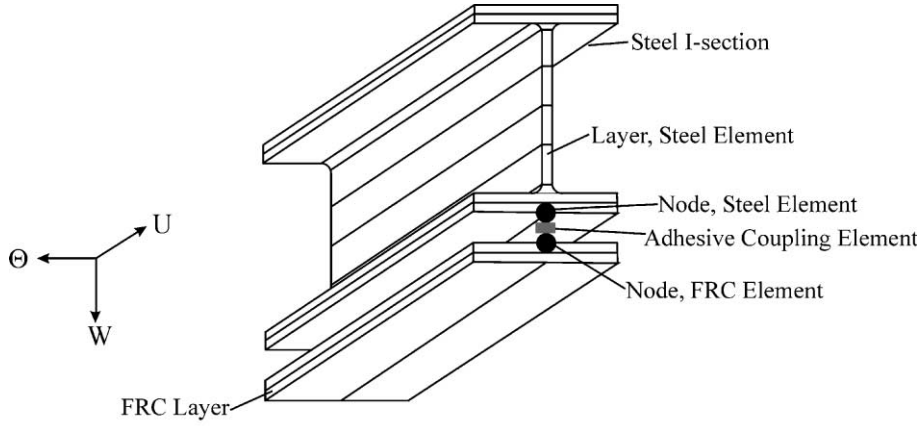


**(a) Assembly of Elements**

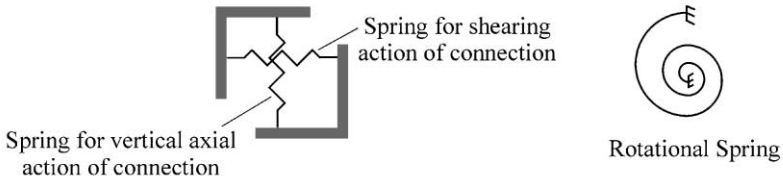


**(b) Details of Coupling Element**

Fig. 7. Assembly of FEs.

between the laminate and I-section owing to the shear deformability of the adhesive. The vertical and rotational springs permit relative increments of the corresponding degrees-of-freedom between the FRC laminate and the steel beam. The stiffness properties allocated to the springs are based on the Shear and Young's moduli, as well as the thickness and length, of the region of adhesive represented by the coupling element. Useful output data from the program include shear-bond stresses in the adhesive, axial strains in the laminate, and vertical deflections of the hybrid member.

### 3.2. Hybrid members used for present study

Two steel I-section–FRC laminate hybrid members are considered in this study. Both hybrid members are single span simply supported. The smaller of the two hybrid members was fabricated and tested in the laboratory, and was also analysed using both the FE program and the present algebraic models.

The larger steel I-section–FRC laminate hybrid member was used to increase the practical value of the shear-bond stress predictions. The geometric and material properties assigned to this member are given in Table 1. The member is compact, so the flanges and web can sustain high compressive strains without experiencing local buckling. It is assumed that sufficient local stiffening is provided to further enhance the compressive strain capacities of the web and flange to at least the maximum values calculated in the present analyses, and also that the member as a whole is restrained against lateral–torsional buckling. Owing to resource limitations, this larger hybrid member could not have been assembled and tested in the laboratory, but confidence had already been gained in the predictive capabilities of the models from comparisons with the measured data for the smaller hybrid member. Note that the adhesives used in practice possess Shear moduli typically in the range 0.4–1.5 kN/mm$^2$. Hence the 0.5 kN/mm$^2$ adhesive Shear modulus chosen (Table 1) for the FE analysis of the larger hybrid member is near the lower end of the range. Since slip between the laminate and the beam becomes more pronounced with reduction in adhesive Shear modulus, and as the algebraic models presented in this paper assume rigid bond between the laminate and the beam, the choice of a low adhesive Shear modulus in the FE analysis permits any compromises inherent in the rigid bond assumption to become clearly manifest.

For the smaller hybrid beam, two concentrated loads were applied within the span, while for the larger specimen a uniformly distributed load (UDL), a seven-point loading arrangement in the span and a single-point loading arrangement in the span were considered in three separate analyses. All non-UDL arrangements for both specimens are shown in Fig. 8. It was found that the disparity in shear-bond stresses, due to the difference between the assumption of rigid bond and the reality of a shear-deformable adhesive layer, increased as the number of point loads reduced, with minimum and maximum disparity for the UDL and the single-point load respectively. In what follows, the results are presented in the order in which this

Table 1
Geometric and material properties of beams used for verification study

| Beam | $A_f$ (mm$^2$) | $A_p$ (mm$^2$) | $b_p$ (mm) | $b_w$ (mm) | $d_w$ (mm) | Span (m) | $t_a$ (mm) | $t_f$ (mm) | $t_p$ (mm) |
|---|---|---|---|---|---|---|---|---|---|
| *Dimensions* | | | | | | | | | |
| LB | 15120 | 4200 | 420 | 21 | 848 | 8 | 1 | 36 | 10 |
| SB | 1285 | 800 | 100 | 6.3 | 187.6 | 4.5 | 4 | 9.6 | 8 |
| | $E_a$ (kN/mm$^2$) | $E_p$ (kN/mm$^2$) | $E_s$ (kN/mm$^2$) | $G_a$ (kN/mm$^2$) | $\sigma_y$ (N/mm$^2$) | | | | |
| *Material properties* | | | | | | | | | |
| LB | 1.4 | 300 | 190 | 0.5 | 275 | | | | |
| SB | 1.85 | 137 | 200 | 0.7 | 301 | | | | |

LB—larger beam (Fig. 8(a)); SB—smaller beam (Fig. 8(c)).

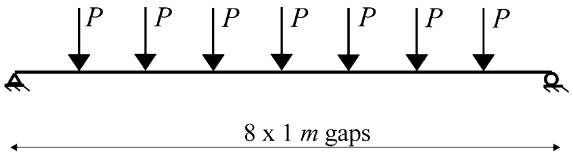


**(a) Larger beam ; Seven point loads in span**

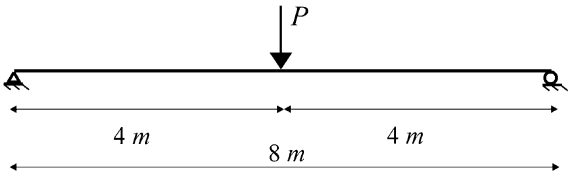


**(b) Larger beam ; One point load in span**

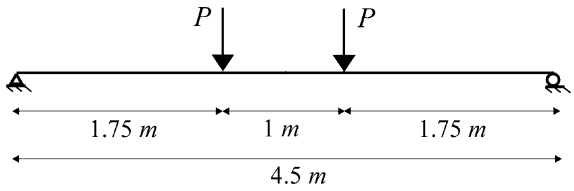


**(c) Smaller beam ; Two concentrated loads in span**

Fig. 8. Loadings considered in verification study.

disparity increases, that is to say, with the UDL considered first, and the minimum number of point loads last. As the UDL was applied to the larger specimen only, the results for this specimen are shown first, with the results for the smaller member shown afterwards. Owing to symmetry about mid-span, all results are presented for only one half of the span of each member. On all plots, the terms FE, ALG and EXP refer to data from the FE analysis, the ALGebraic models and the laboratory EXPeriments respectively.

### *3.3. Results for larger hybrid beam*

#### *3.3.1. Uniformly distributed loading*

Eq. (1) can be re-expressed to show that the shear-bond stress is directly proportional to the axial gradient of the force in the FRC laminate. Hence, it is instructive first to consider the axial variation of laminate force in the elastic–plastic regions, and to establish how this variation is influenced by the corresponding variation of tensile force in the adjacent steel. To that end, for an applied load of 5960 kN, Fig. 9(a) shows the axial variation of total tensile force below the neutral axis of the hybrid member, while Fig. 9(b) shows the individual contributions to this total force variation from each of the FRC laminate and the steel. On both plots, the initiation point for each elastic–plastic phase defined in Fig. 2 is given as P1, P2 to mean start of phase 1, 2, and so on. Note that phase 5 ends at mid-span. In the following discussion, the term RI is used to mean "rate of increase".

Fig. 9(a) shows that the total tensile force increases monotonically towards mid-span. In Fig. 9(b), as we proceed from phases 1 and 2 to phase 3, a distinct increase in nonlinearity of the steel force variation is evident. This is due to the strong influence of axial stress redistribution through the steel tension flange in

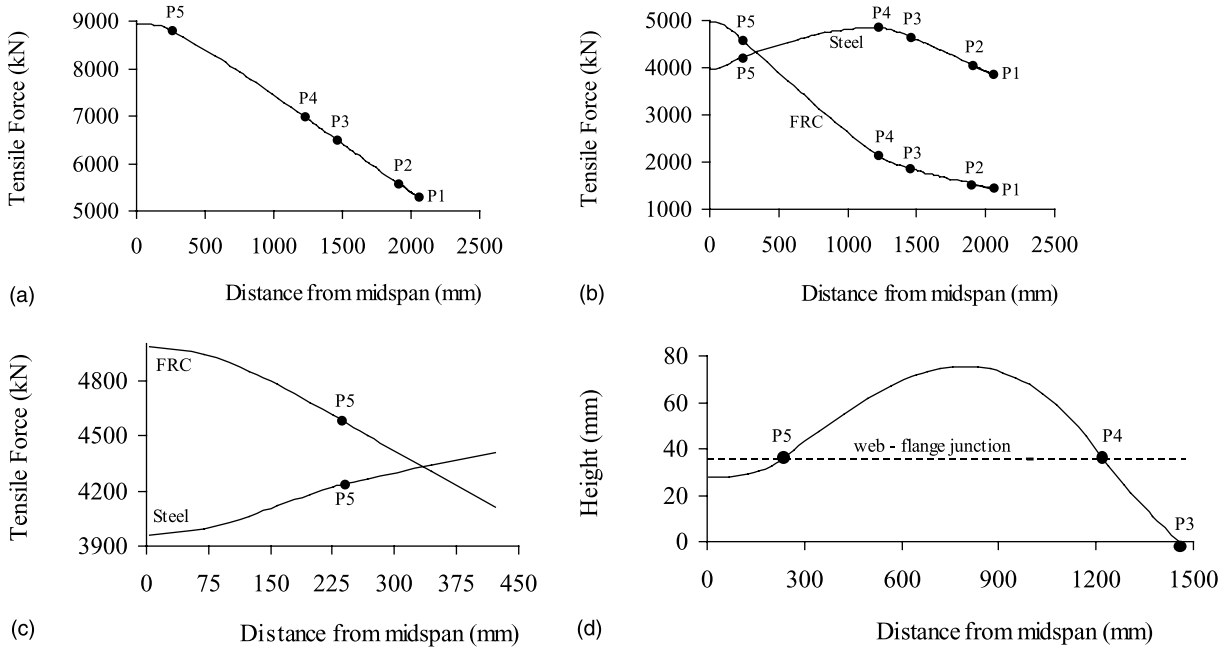


Fig. 9. Tensile actions along elastic–plastic zone of larger beam at 5960 kN UDL: (a) total tensile force; (b) steel and FRC tensile forces; (c) magnification of steel and FRC forces near mid-span; (d) height of tensile plastic zone.

phase 3. The steel tension flange is of much greater area than, and is further away from the neutral axis than, the tension web. Changes in this steel tension flange force, due to redistribution, will thus have the dominant influence on changes in the overall steel tension force. Hence as the tension flange yields incrementally during phase 3, the progressive reduction in RI of the steel flange force will cause a corresponding progressive decrease in RI of overall steel tension force, until there is zero RI of this overall steel force when the entire flange has yielded. It is for this reason that, in Fig. 9(b), the phase 3 zone shows a nonlinear variation of steel force down to zero gradient (maximum force) at the transition to phase 4. Since the RI of *total* tension force (Fig. 9(a)) is high in phase 3, this rapid *reduction* in RI of steel force must be compensated for by a rapid *rise* in RI of force in the laminate, as is clearly evident from Fig. 9(b). Therefore, sharp increases in shear-bond stress can be expected in phase 3.

During phase 4, as the drop of the neutral axis reduces the area of tension web, and as the tension flange carries a constant (yield) force, the overall steel tension force decreases progressively, as seen in Fig. 9(b). Early on in phase 4, this effect stimulates further RI of force in the laminate (to increase total tension force (Fig. 9(a))), which in turn should lead to moderate increases of shear-bond stress. However, in the very advanced stages of phase 4, near mid-span, the flattening of the moment diagram induces decreasing gradients in the tensile force variations of Fig. 9(a) and (b). This should lead to reduction of shear-bond stress in the very latter stages of phase 4. In phase 5 this general trend of decreasing gradient of the steel force variation to zero at mid-span continues, except for a pronounced inflection in this variation near the transition (point P5 in Fig. 9(b)) from phase 4 to phase 5. This inflection is shown in more detail in Fig. 9(c) and owes its existence to redistribution of axial stress in the steel tension flange in phase 5. This redistribution is similar to that described above for phase 3, except that the elastic–plastic boundary in the steel tension flange is now moving outwards in phase 5 as opposed to inwards in phase 3. Hence, whereas the overall steel force experienced reduced rates of *increase* during phase 3, it now experiences higher rates of

*loss* (hence the rapid dip just after the P5 inflection in Fig. 9(b)) in phase 5. This higher rate of loss in steel force early on in phase 5 must be offset by an opposing increased rate of increase in the FRC force (Fig. 9(b)), to ensure that the total tensile force continues to rise. Herein lies the explanation of the slight upward inflection in the FRC force curves of Fig. 9(b) and (c) near P5. This effect is local to the region of phase 5 very near the transition from phase 4, and should lead to a local increase in shear-bond stress over a short length of phase 5 after the transition. Elsewhere within phase 5, the reduction of all force gradients to zero resumes towards mid-span; which should give a similar monotonic reduction of shear-bond stress to zero. The upshot of these effects is that, in proceeding from the final stage of phase 4 through phase 5, the shear-bond stress should initially decrease, then increase rapidly over a short length, and finally decrease to zero at mid-span. These shear-bond stress predictions are confirmed in Fig. 10(a) and (d), discussed below.

Fig. 9(d) shows the axial variation in height of the tensile plastic zone at 5960 kN applied load. The initiation point for each elastic–plastic phase is identified by P3, P4, P5, as in Fig. 9(a)–(c). The variation is exactly as described for the different phases in Section 2.3 and in Fig. 2. In particular, note that the earlier prediction of yield of the tension web first away from, and then back towards, the tension flange during phase 4 is clearly evident in Fig. 9(d). The phase 5 movement of the elastic–plastic boundary outwards through the tension flange has also been correctly predicted.

Fig. 10(a) shows the FE-predicted shear-bond stress distributions along the beam at four different load levels. The lowest load level corresponds to fully elastic behavior, while the three highest loads represent increasing levels of elastic–plastic behavior of the member. The highest load level of 5960 kN is that considered in Fig. 9 and discussed above. For fully elastic behavior, the expected linear variation of shear-bond stress, with maximum value at the supports and zero at mid-span, and which mimics the shear force distribution, is predicted. The magnitudes of the elastic shear-bond stresses are virtually identical to those

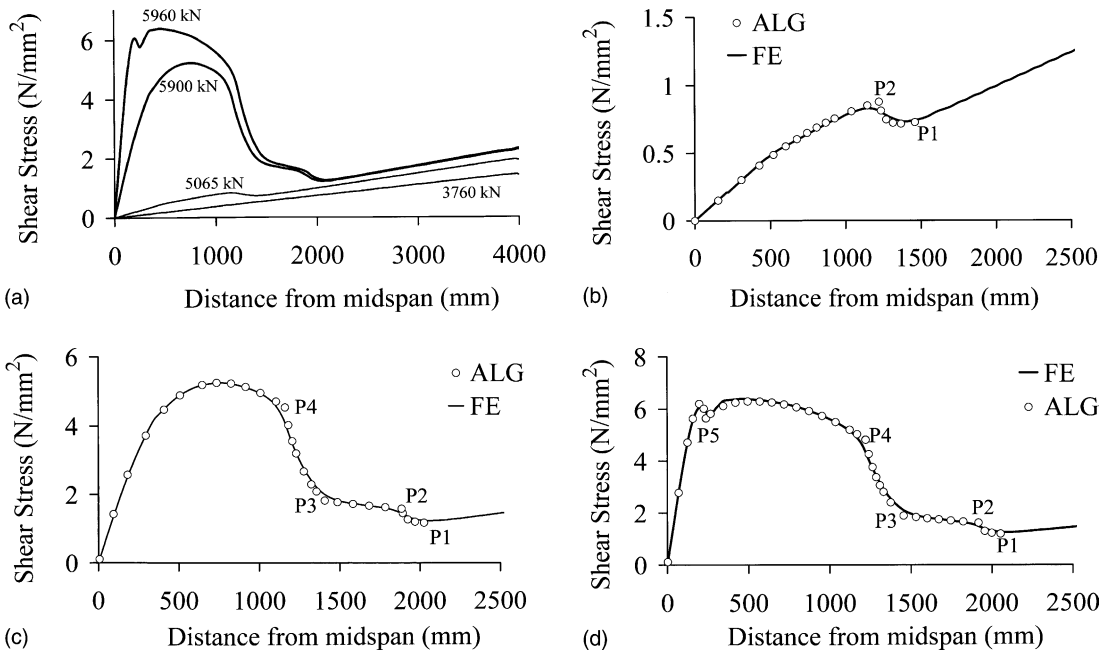


Fig. 10. Shear-bond stresses along larger beam under UDL: (a) FE predictions only; (b) 5065 kN load; (c) 5900 kN load; (d) 5960 kN load.

predicted from the standard beam-theory formula discussed in Section 2.2. However, as elastic–plastic behavior becomes increasingly pronounced, the shear-bond stress variations along the elastic–plastic zones become progressively nonlinear, even though the shear force variation remains linear. For each of the three uppermost plots, the elastic–plastic zone is the region over which nonlinear shear-bond stress variation occurs. It is seen that this region progresses outwards from mid-span with increase in load. Each nonlinear variation shows a peak of shear-bond stress near mid-span, with the location along the member of this peak stress moving incrementally towards mid-span as the load increases. This contrasts sharply with elastic behavior, where the peak shear-bond stress occurs at the supports and is very low near mid-span.

In Fig. 10(b)–(d), each of the three upper shear-bond stress variations of Fig. 10(a) is compared in turn with the corresponding predictions from the algebraic models of this paper. Good agreement is evident. On each plot, the initiation of each elastic–plastic phase is identified as was done in Fig. 9. In Fig. 10(d), the shear-bond stress variation matches that predicted in the previous discussions based on the changes in behavior from one elastic–plastic phase to the next (Fig. 9(a)–(c)). This underlines the fundamental importance of the phases in dictating the elastic–plastic shear-bond stress variations. Specifically, note that the sharp increase in stress predicted in phase 3, and the drop then rise and subsequent drop in stress predicted in the transition from phase 4 through phase 5, both occur in Fig. 10(d). As explained previously, axial stress redistributions within the steel tension flange lie at the heart of both these rapid shear stress variations.

Given that the FE analysis and the present modeling employ adhesive shear connections at opposite ends of the shear stiffness spectrum, the excellent agreement evident in Fig. 10(b)–(d) suggests that, under uniformly distributed loading, the magnitudes of the shear-bond stresses developed during elastic–plastic behavior are not very sensitive to the Shear modulus of the adhesive.

*3.3.2. Seven-point loading*

For the seven-point load arrangement of Fig. 8(a), the FE-predicted shear-bond stress distributions along the beam for a fully elastic stage of behavior and for an advanced stage of elastic–plastic behavior are given in Fig. 11(a) and (b) respectively. In Fig. 11(b), where predictions from the algebraic models of this paper are provided for comparison, the peak moment in the member is equal to that considered for the uniformly distributed loading in Fig. 10(d). On Fig. 11(a), the shear-bond stresses predicted from the standard beam-theory formula (Section 2.2) are also plotted (labeled BT on Fig. 11(a)). Fig. 11(a) shows that conventional beam theory compares well with the FE analysis, except in the immediate vicinities of the point loads where beam theory predicts an abrupt change in shear-bond stress, while the FE analysis predicts a smooth variation of bond stress. When the Shear modulus of the adhesive was increased in the FE analysis, the predicted transition length between adjacent "steps" decreased and approached the abrupt change for the rigid adhesive.

Fig. 11(b) shows that the predictions from the present algebraic models also approximate closely to the FE-predicted results, except very near the point loads. The disparities are negligible at the locations of the off-centre point loads, but they become progressively pronounced as the mid-span point load is closely approached. The peak FE-predicted and algebraically predicted shear-bond stresses are circa 9 and 20 $N/mm^2$ respectively; a factor of 2 apart. As mid-span is approached, the FE predictions reach a peak and then decrease sharply over a short length so that the zero shear-bond stress condition at mid-span is satisfied, while the algebraically predicted shear-bond stresses increase monotonically towards mid-span and drop abruptly to zero at mid-span. The sharp change in shear-bond stress circa 1 m from mid-span occurs near a point load. Where the algebraic and FE models agree near mid-span, another sharp increase in shear-bond stress is evident; again due to axial stress redistribution within the steel tension flange (phase 5) stimulating large force increments in the FRC laminate over short distances.

In both Fig. 11(a) and (b), the difference in predicted shear-bond stresses near point loads is a direct consequence of the shear flexibility of the adhesive, which has been ignored in beam theory and in the

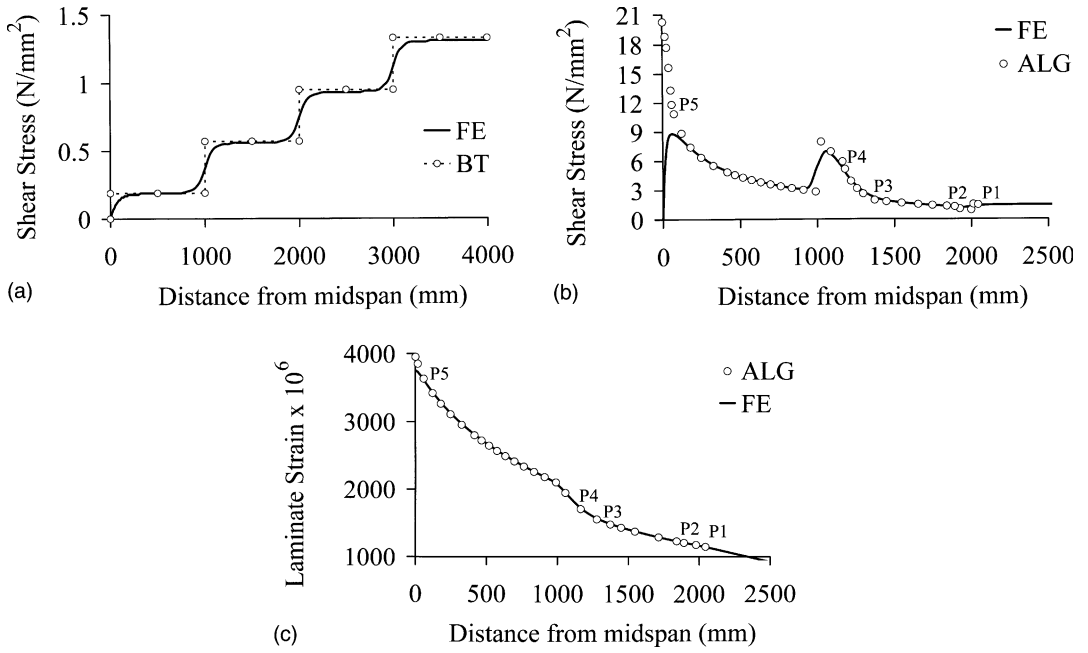


Fig. 11. Larger beam under load of Fig. 8(a): (a) shear-bond stresses at 3330 kN load; (b) shear-bond stresses at 5215 kN load; (c) laminate strains at 5215 kN load.

present algebraic models. However, in Fig. 11(b), since the FE and algebraic analyses compare well at short distances away from the point loads outwards, it may be that a separate algebraic method incorporating slip between the FRC laminate and steel beam can be developed to predict shear-bond stresses in very short elastic–plastic zones near point loads. The analysis set out in this paper may then be applied elsewhere in the elastic–plastic region. The analysis incorporating slip will, by necessity, be far more complex than that given here. By limiting the requirement for development of this more complex analysis to a small zone near the point loads, the algebraic effort is reduced.

Fig. 11(c) compares the FE and algebraic axial strains at the mid-thickness of the laminate for the elastic–plastic load level considered in Fig. 11(b). The results compare well, except in the immediate vicinity of mid-span where the strain differences are palpable (though not gross), but the difference in strain gradients is large. Given the link in Eq. (1) between strain gradient and shear-bond stress, this consistency of trends between laminate strain gradient and shear-bond stress variation points to high degrees of self-consistency within the FE analysis and within the algebraic models.

### *3.3.3. Single-point loading*

For the single mid-span point load of Fig. 8(b), the FE-predicted and algebraically predicted shear-bond stresses along the member are compared in Fig. 12 for a load level giving the same mid-span moment in the member as considered for Fig. 11(b). Again, Fig. 12 shows good agreement in the nonlinear zones except very near the mid-span point load, with peak FE and algebraic stresses of 26 and 80 N/mm$^2$ respectively. Clearly, the effect of shear-lag in the adhesive very near point loads must be considered in future work. Note also the highly nonlinear disparity between the shear force variation, which is a horizontal line, and the elastic–plastic shear-bond stress variation of Fig. 12.

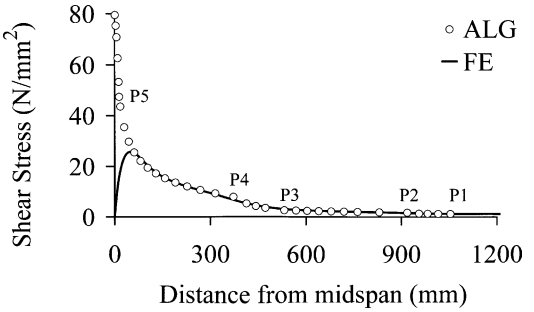


Fig. 12. Shear-bond stresses along larger beam under single mid-span point load of 2980 kN.

### 3.4. Laboratory-tested hybrid member

The geometric and material properties of the laboratory-tested hybrid member are given in Table 1. During the lab test, the member was restrained by scaffolding to inhibit lateral–torsional buckling. The loading arrangement for this member is shown in Fig. 8(c).

In Fig. 13(a), the FE-predicted, algebraically predicted and laboratory-measured axial strains on the outer surface of the laminate are compared for 127.2 kN total load on the member, a load level well into the elastic–plastic regime of behavior of the member. The steel compression flange of the beam buckled soon after the data of Fig. 13(a) were recorded. The algebraically predicted elastic–plastic zones, as defined in Fig. 2, are identified in Fig. 13(a) as done for Fig. 9. It is seen that both sets of predictions compare well with the measured data. However note that while the gradients of the FE-predicted and measured strains are similar, the gradients of the algebraically predicted strain variations are notably higher than the others

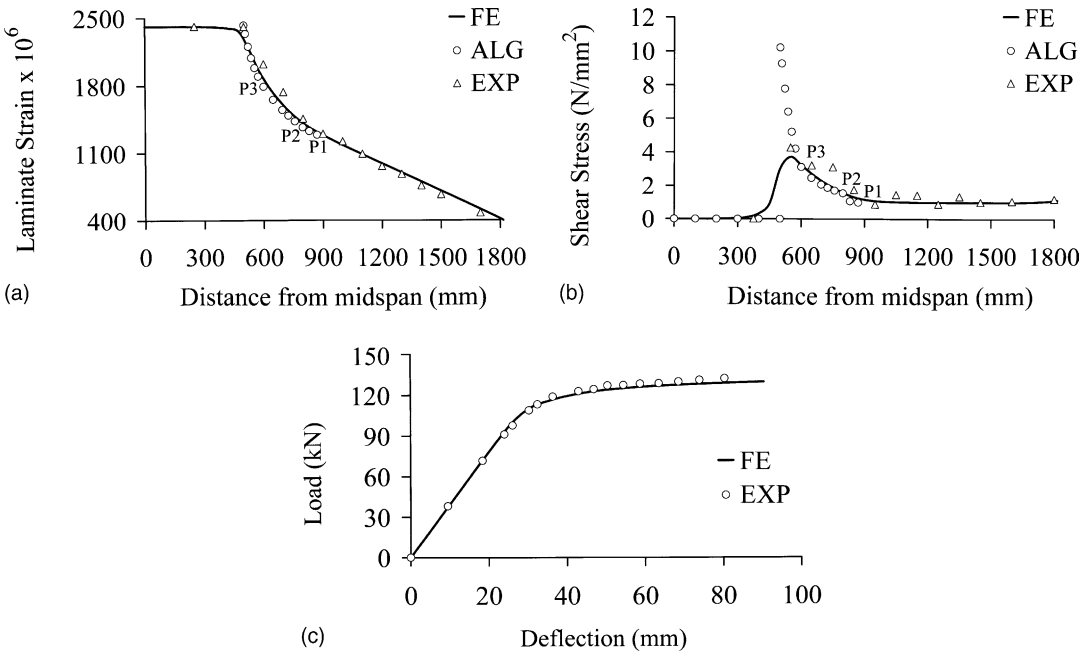


Fig. 13. Smaller beam under the two concentrated span loads of Fig. 8(c): (a) laminate outer surface strains at 127.2 kN load; (b) shear-bond stresses at 127.2 kN load; (c) load vs midspan deflection.

very near the location of the point load and gradually approaches the other gradients as the member is traversed away from the span point load towards the supports. Hence, again, it is anticipated that the algebraically predicted shear-bond stress variations will be similar to the corresponding FE-predicted and experimentally determined variations except in the immediate vicinity of the point load. This is confirmed in Fig. 13(b) where, apart from the disparity over only a 50 mm length on the support side of the span concentrated load, the three shear-bond stress variations agree well. In the zone of disparity, the peak shear-bond stresses are circa 4 N/mm$^2$ for the FE and experimental variations, and 10 N/mm$^2$ from the algebraic analysis. In Fig. 13(b), note also that while the algebraically predicted shear-bond stresses drop abruptly to zero at the edge of the constant moment region, the FE-predicted stresses decrease gradually to zero over roughly 250 mm within the constant moment zone; another effect of shear-lag in the adhesive.

The experimentally determined shear-bond stresses of Fig. 13(b) were calculated by applying the approximate form of Eq. (1) to the experimental data of Fig. 13(a). Strictly speaking, Eq. (1) should be applied to the axial strains at the mid-thickness of the laminate. However, by necessity, the measured strains of Fig. 13(a) were obtained from gauges bonded to the outer surface of the laminate. Since the section neutral axis moves towards the laminate in elastic–plastic zones, and as the laminate is itself relatively (8 mm) thick, the axial strain at the outer surface of the laminate is perceptibly greater than that at the mid-thickness of the laminate. These facts together mean that the experimental shear-bond stresses of Fig. 13(b) are slightly greater than the true values. This brings the test data into even closer agreement with the (particularly FE) predicted results. In Fig. 13(b), the somewhat high experimentally derived data point at 750 mm from mid-span may well have been due to a small debond giving rise to a local shear-bond stress concentration.

Further evidence of the realism of the FE predictions can be seen in Fig. 13(c), where the FE-predicted and laboratory-measured mid-span deflections for the hybrid beam are compared. It is seen that the excellent correlation extends well into the nonlinear regime.

## 4. Discussion—capabilities of algebraic models

The good agreement between FE-predicted and measured data for the laboratory-tested hybrid member gave confidence in the FE predictions as a credible base for comparison of results when alternative members under various load types are considered. Hence the comparisons of the previous sections suggest that the algebraic models presented in this paper provide robust predictions of the shear-bond stresses in elastic–plastic zones when uniformly distributed loading is applied. When point loads are applied, the algebraic models also provide very good predictions of shear-bond stress, except in the immediate vicinity of the point loads, where the algebraic predictions were found to be up to three times the corresponding FE predictions. Further work should focus on introducing the Shear modulus of the adhesive and on permitting slip between the laminate and the steel beam in the algebraic analysis. This work may focus on the short region of disparity very near the point loads. This would serve to further strengthen the predictive capabilities of an already powerful algebraic modeling. Such model enhancement is currently underway at the University of Bristol.

## 5. Conclusions

Algebraic models have been presented to predict the shear-bond stresses in elastic–plastic zones of hybrid structural members comprising I-section steel beams and adhesively bonded FRC laminates. Advanced features of the models include the representation of both the vertical movement of the neutral axis and the progressive spatial plastification of the member with increase in load, along with the ability to

predict shear-bond stresses under any form of external loading. The models clearly illustrate that there is a highly nonlinear relationship between shear-bond stress and shear force during elastic–plastic behavior. Predictions from the models have been compared with corresponding predictions from a FE analysis which models the adhesive layer as a shear-flexible connection, and with experimental data. Throughout this verification study, the high degree of nonlinearity of the shear-bond stress variations along the elastic–plastic zones of the hybrid members, which contrasts sharply with the linear variations of shear force, has been evident.

Both distributed loads and point loads were applied to the hybrid members in the verification study. When distributed loads were applied, the algebraic models were found to provide excellent predictions of the shear-bond stresses throughout the entire elastic–plastic zone. Axial stress redistribution within the tension steel flange was found to induce rapid axial variation of shear-bond stress in the adhesive layer. For point loads, the algebraic predictions of shear-bond stress in elastic–plastic zones were also robust, except in the immediate vicinities of the point loads, where the algebraic predictions were found to be up to three times those which develop in practice. The source of the disparity has been identified as the assumption of infinite shear stiffness of the adhesive layer in the algebraic models. This attracts higher shear-bond stresses to the adhesive layer in the algebraic model than the finite shear stiffness of the adhesive layer permits in practice. Algebraic models which minimize these disparities near point loads are under development at the University of Bristol.

## Acknowledgements

The work described in this paper was conducted during the tenure of an Advanced Research Fellowship awarded to the author by the University of Bristol. The experimental data of Fig. 13 were obtained from tests by the author and funded by Railtrack Ltd. through the efforts of Mr. Brian Bell of Railtrack Ltd. and Dr. Sam Luke of Mouchel International Consultants. These opportunities are gratefully acknowledged.

## References

Hollaway, L.C., Leeming, M.B., 1999. Strengthening of Reinforced Concrete Structures using Externally-Bonded FRP Composites in Structural and Civil Engineering. CRC Press LLC, Boca Raton, FL.

Kim, D.K., Sebastian, W.M., 2002. Parametric study of bond failure in concrete beams with adhesively-bonded fibre reinforced polymer plates. Magazine of Concrete Research 54 (1), 47–59.

Malek, A.M., Saadatmanesh, H., Ehsani, M.R., 1998. Prediction of failure loads of R/C beams strengthened with FRP plate due to stress concentration at plate end. Structural Journal of the American Concrete Institute 95 (1), 142–152.

Roberts, T.M., 1989. Theoretical study of reinforced concrete beams strengthened by externally bonded steel plates. Proceedings of the Institute of Civil Engineers, Part (2) 87, 39–55.

Sebastian, W.M., 2001. Significance of midspan debonding failure in FRP-plated concrete beams. Journal of Structural Engineering, American Society of Civil Engineers 127 (7), 792–798.

Sebastian, W.M., McConnel, R.E., 2000. Nonlinear FE analysis of steel–concrete composite structures. Journal of Structural Engineering, American Society of Civil Engineers 126 (6), 662–674.

Täljsten, B., 1994. Plate bonding: Strengthening of existing concrete structures with epoxy bonded plates of steel or fibre inforced plastics. Doctoral Thesis, Lulea University of Technology, Sweden.

Triantafillou, T.C., Plevris, N., 1992. Strengthening of RC beams with epoxy-bonded fibre composite materials. Materials and Structures, Paris 25, 201–211.